Contents lists available at ScienceDirect

International Journal of Heat and Mass Transfer

2-D and 3-D modulated porous coatings for enhanced pool boiling

D.H. Min [a], G.S. Hwang [a], Y. Usta [b], O.N. Cora [b], M. Koc [b], M. Kaviany [a],*

[a] Department of Mechanical Engineering, University of Michigan, Ann Arbor, MI 48109-2125, USA
[b] NSF IUCRC – Center for Precision Forming (CPF), Department of Mechanical Engineering, Virginia Commonwealth University (VCU), Richmond, VA, USA

ARTICLE INFO

ABSTRACT

A new fabrication method (hot-powder compaction) is developed to readily make 2-D and 3-D modulated coatings for enhanced pool-boiling performance. The modulated coatings are 2-D and 3-D stacks with different height, width, and pitch (modulation wavelength), and made with different particle diameters and porosities. The maximum measured critical heat flux (q_{CHF}) of 2-D and 3-D modulated coatings are 3.3 and 2.0 times that of the surface without coatings (plain). As expected from the hydrodynamic stability theory, the experimental results for 2-D coatings are similar to 3-D coatings and show that q_{CHF} strongly depends on the modulation wavelength, while particle diameter and porosity have a little effects. The results also suggest that a stack aspect ratio (height to pitch) larger than unity is needed for modulation enhancement of the critical heat flux.

1. Introduction

Modulated surface coatings with geometric variations have been studied for enhancing critical heat flux (q_{CHF}) and reducing the superheat across the wick in pool boiling [1–9]. The enhancement is attributable to the combinations of complex flow in the liquid–vapor interface, the solid and fluid thermophysical properties and the geometric coating parameters such as stack height l, particle diameter d_p and porosity ϵ. Prior to q_{CHF}, the liquid–vapor counter flow is balanced. Once q_{CHF} is reached, this liquid–vapor two-phase flow becomes unstable and liquid supply lags the vapor escape which results in the surface dry-out (sudden increase in surface temperature). Zuber developed the q_{CHF} model for a plain surface by using the hydrodynamic stability theory [10], where q_{CHF} can be related to the modulation wavelength λ_m [11]. Previously, 3-D modulated porous coatings were fabricated using micromachined graphite molds which were filled with copper particles and sintered. Then the modulated layer was sintered to the surface. Using these, the measured q_{CHF} reached about 3.3 times that of a plain surface [11]. Assuming the modulation wavelength λ_m is the pitch between 3-D stacks, the result is well predicted by the Zuber theory. However, the bonding between the 3-D porous layer and the copper substrate is not ideal and the contact resistance can develop easily. In order to improve this bonding, 2-D and 3-D porous coatings are produced here by hot-powder compaction.

In this study, the new fabrication method is introduced along with the pool-boiling experimental procedures. The experimental heat transfer results for the 2-D, and 3-D modulated porous coatings are presented, compared with the results from previous studies [11,12], and discussed.

2. Experiment

2.1. Fabrication of coatings

The surface coatings used in this study are prepared by hot-powder compaction, and the detailed description of tooling and fabrication procedure are shown in Fig. 1(a) and (b). The apparatus of hot-powder compaction mainly consists of a universal MTS machine (Instron HVL5596) with a loading capacity of 2000 kN, compaction die set (lower die/punch, upper die, container), heating elements, control and DAQ system. In order to conduct the tests, the compaction die set, which has an upper die and lower punch of 55 mm in diameter, was designed and manufactured out of H13 tool steel. The detailed hot-powder compaction procedure is shown in Fig. 1(b). (i) At the beginning, lower punch (with grooves/channels) was placed 0.7 mm lower than the die/container's upper surface to have a cavity. (ii) This cavity was filled with copper powders. A thin copper substrate of 0.4 mm thickness was placed on top of powders so that it levels with the upper surface of the container. (iii) Then, the upper die was inserted against the thin substrate. This entire region was covered with crushed charcoal to reduce the oxidizing effect during heating and warm compaction. Heating of the entire die set was achieved through band heaters around upper and lower dies. Two thermocouples were used to measure and record the temperature on the dies. The selection of the thermocouple placement was determined via

* Corresponding author. Tel.: +1 734 936 0402; fax: +1 734 615 6647.
E-mail address: kaviany@umich.edu (M. Kaviany).

Nomenclature

A	area (m^2)
d_p	particle diameter (m)
g	gravitational acceleration (m/s^2)
Δh_{lg}	enthalpy of vaporization (J/kg)
l	stack height (m)
p	(compaction) pressure (Pa)
q	heat flux (W/m^2)
R	base radius (m)
T	temperature (K)
w	stack width (m)

Greek symbols
δ	coating base thickness (m)
ϵ	porosity
λ	wavelength (m)

ρ	density (kg/m^3)
σ	surface tension (N/m)

Subscripts
b	base of surface
CHF	critical heat flux
g	gas (vapor), gas flow
K–H	Kelvin–Helmholtz
l	liquid
lg	liquid–vapor, or saturation
m	modulation
p	particle, or plain
R–T	Rayleigh–Taylor
s	saturation

the finite element heat transfer analysis. (iv) Once both upper and lower punches reached the desired temperature level (350, 425 or 500 °C), the upper punch was moved down in a controlled manner by the Instron machine's load/displacement control systems to the desired level of pressure. After each test, specimens were taken out of the die and sintered at a temperature of 900 °C for 1 h. During sintering, crushed charcoal was used as controlling atmosphere. Change of color in the copper porous surface was taken as an indication of oxidation, and no oxidation was observed. In all experiments, Cu powders of nominally 200 μm in diameter (61 Copper Shot, supplied by Acupowder Co.) were used. 90% of the powders were in the range of 150–249 μm in diameter. Under the guidance of previous experimental results [13], additional preliminary tests were conducted to determine experimental limitations in terms of minimum temperature (T, 350 °C) and minimum pressure (p = 15

MPa) to yield sound specimens with micro-scale porous channels on the 55 mm surface area. The upper boundaries of the experimental conditions were selected as 500 °C of temperature and 50 MPa of pressure due to the limitations of the tool steel used and the load carrying capability of the experimental apparatus.

Fig. 2 shows the SEM micrographs of 2-D and 3-D modulated coatings. In the 2-D modulated coatings, the geometry is divided into (a), (b), and (c) according to the aspect ratio and particle diameter. In the 3-D modulated coating, (d), (e), and (f) are fabricated by hot-powder compaction, while (g) is by graphite mold and sintering from [11]. Fig. 3 shows the geometric parameters for the modulated coatings. The specifications for the 2-D and 3-D modulated coatings are summarized in Table 1.

2.2. Porosity measurement

Compacted and sintered specimens were cut into four pieces for porosity and dimensional measurement and analyses. The sections of each specimen cut for the porosity measurements were sunk into bakelite and subjected to polishing operations. After sandpapering and polishing with 1 μm diamond paste, each specimen section was cleaned using ultrasonic cleaning to remove the small burrs and displaced powders into the pores resulted from polishing operation.

Microscopic pictures of each sample were taken after ultrasonic cleaning to measure the porosity percentage by image processing using commercially available software called Image-J. The pictures taken for the porosity measurements were converted to black and white (binarizing) first.

Then bumpy/channel surface boundaries were selected, and the ratio of the black color area to white color area was calculated and recorded. Average minimum, and maximum values for each sample and for each experimental condition were then calculated. As expected, there is a descending and exponential slope of the porosity with an increasing pressure, independent of the aspect ratio or the surface geometry. The temperature, at least within the experimental range, has almost no effect on porosity at high pressure levels. However, porosity decreases with an increasing temperature at low pressure levels. The minimum and maximum porosity percentages were recorded as 21.1% and 42.1%, respectively. The apparent density of the powders used in the tests was given as 4.5–5.5 g/cm^3 by the copper powder manufacturer (Acupowder Co.). It was declared as 5.01 g/cm^3 in the product certificate. This density value corresponds to the porosity value of 43.8% from the basic apparent density calculations. Based on these values, it can be concluded that the deformation level applied during the experiments was in the range of 4–20%.
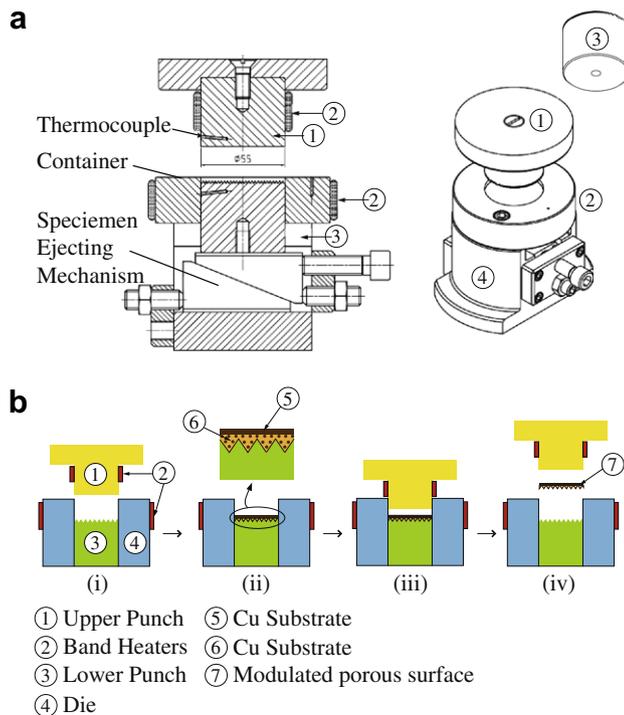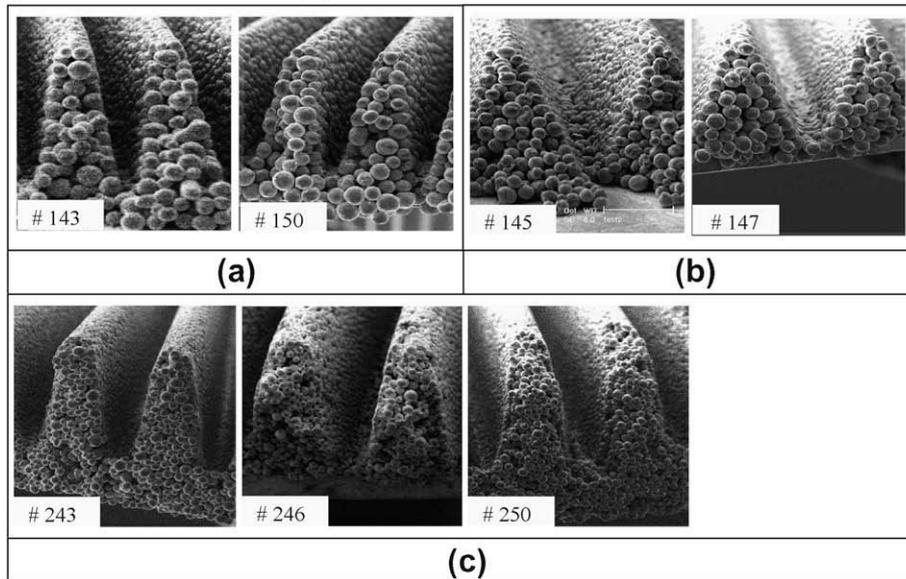

Fig. 1. (a) Description and part features of the tooling for hot-powder compaction. (b) Apparatus and procedure for the production of 2-D and 3-D surfaces.

Thermocouple
Container
Specimen Ejecting Mechanism

① Upper Punch   ⑤ Cu Substrate
② Band Heaters   ⑥ Cu Substrate
③ Lower Punch   ⑦ Modulated porous surface
④ Die

[2-D Modulated Porous Coatings]

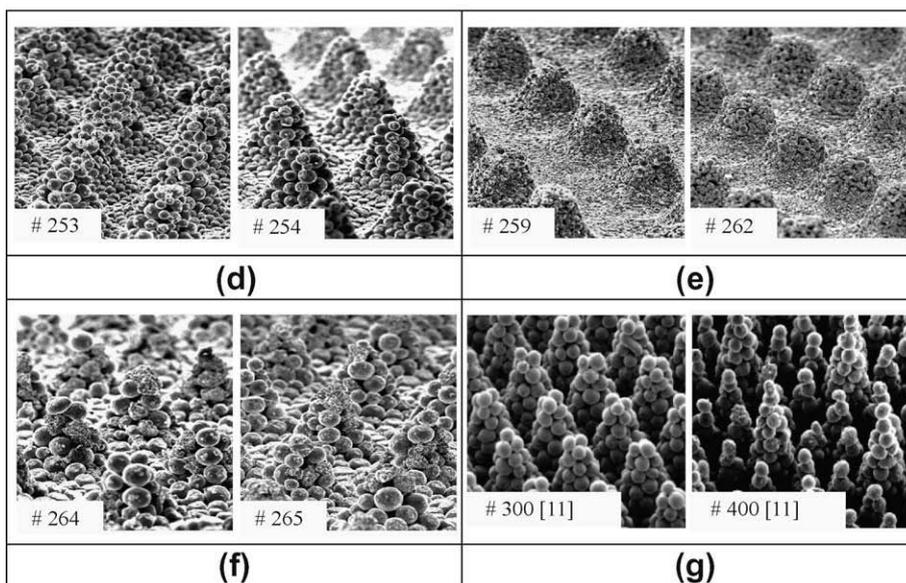
[3-D Modulated Porous Coatings]

Fig. 2. SEM micrographs of 2-D and 3-D modulated porous coatings. There are variations in stack pitch (modulated wavelength), width, and height, in addition to particle diameter and porosity.
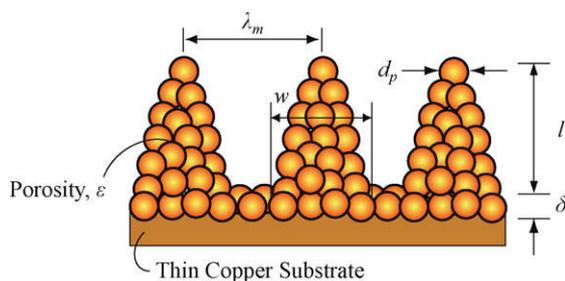

Fig. 3. Geometric parameters of modulated coatings.

2.3. Pool-boiling experiment

The description for the experimental apparatus and procedures is reported in previous studies [11,12]. Pentane is used for the experiment at atmospheric pressure. All porous coatings are already bonded to a thin copper substrate (disk) of 5.08 cm diameter, and are then soldered on a cylindrical solid copper base of same diameter and 4.5 cm in height. Then, this test piece is attached to a large insulated copper thermal mass by clamping plates. A high thermal conductivity paste is used to reduce the thermal contact resistance between the copper base and thermal mass. A pyrex glass reservoir with two concentric cylinders and a stainless steel plate is fabricated to hold the liquid pool. A copper pipe condenser and a flexible plastic cap are used to close the system and maintain atmospheric pressure. Two electrical heaters of 1.3 kW and 1.0 kW are used to provide heat to the lower half of the insulated copper thermal mass. The insulation along the outside of thermal mass allows the heat flows through the top half of the thermal mass and then through the test piece. A pyrex glass reservoir is wrapped with a flexible guard heater to maintain the reservoir temperature

Table 1
2-D and 3-D modulated porous coatings fabricated using a hot-powder compaction process [13].

Coatings	$\langle d_p \rangle$ (μm)	$\langle \epsilon \rangle$	$\langle l \rangle$ (mm) (± 0.1)	$\langle w \rangle$ (mm) (± 0.1)	λ_m (mm) (± 0.1)	δ(μm)	p (MPa)	T (°C)
2-D								
#143	200	0.36 ± 0.2	2.0	1.0	1.0		25	350
#145	200	0.40 ± 0.2	2.0	1.7	1.9		15	350
#147	200	0.27 ± 0.2	2.0	1.8	1.9		50	350
#150–152	200	0.29 ± 0.2	1.7	1.0	1.0		50	350
#243	100	0.22 ± 0.1	1.8	1.0	1.0		50	350
#246	100	0.28 ± 0.2	1.7	1.0	1.0		15	425
#250	100	0.25 ± 0.4	1.8	1.0	1.0		25	350
3-D								
#253	100	0.25 ± 0.4	0.71	0.6	0.83	172	50	500
#254	100	0.25 ± 0.4	0.71	0.6	0.83	172	50	500
#259	45–53	0.31 ± 0.4	0.71	0.66	0.93	109	50	425
#262	45–53	0.31 ± 0.4	0.71	0.63	0.93	109	50	425
#264	106–150	0.24 ± 0.4	0.71	0.60	0.9	123	50	500
#265	106–150	0.24 ± 0.4	0.71	0.53	0.9	123	50	500
#300 [11]	200	0.40	1.2		1.53			
#400 [11]	200	0.40	1.0, 1.8		1.40			

close to the saturation temperature of the pentane. Five E-type thermocouples are aligned in axial direction, two in the thermal mass and three in the test piece. From the surface where the porous coatings are bonded, one of the three thermocouples is located 2 mm below and set apart 1 cm from the others. These temperatures are used to evaluate the thermal conductivity of the copper test piece and determine the heat flux by Fourier's Law. A thermocouple located above the porous coating is used to measure the saturation temperature of pentane. Since the porous coatings are bonded to the test piece, the temperature underneath the coatings is determined by extrapolation of the heat flux. In pre-CHF regime, each temperature is measured simultaneously by observing constant temperatures (quasi-steady state) from each thermocouples. The heat flux and the saturation temperatures are defined by using the average temperatures over 2 min. The critical heat flux is assumed to be occurred before the sudden temperature rise by film boiling. Almost 10–11 data per each surface has been obtained for the heat flux q and the surface superheat $T_s - T_{lg}$ up to the critical heat flux q_{CHF}. The measured data are listed in Table 2.

Table 2
Measured q_{CHF} and $T_s - T_{lg}$ for 2-D and 3-D modulated porous coatings.

Coatings	Symbol	$T_s - T_{lg}$ (°C)	q_{CHF} (kW/m²)
2-D			
#143	⊙	25.2	707
#145	□	31.7	694
#147	▽	22.2	611
#150	△	12.6	709
#151	◇	16.5	750
#152	◁	15.9	765
#243	▷	14.0	638
#246	◉	13.5	679
#250	⊗	17.4	815
3-D			
#253	■	6.87	482
#254	▼	5.85	460
#259	▲	6.96	375
#262	◆	6.73	491
#264	◀	7.50	399
#265	►	6.36	471
#300 [11]	⊕	16.0	712
#400 [11]	⊖	22.0	762

3. Results and discussion

The effects of porosity ϵ, particle diameter d_p, and modulation wavelength on q_{CHF} and surface superheat are studied using 2-D and 3-D modulated coatings fabricated by hot-powder compaction process [13].

3.1. Effect of porosity

Surfaces #143, #145, #147, #150, #243, #246, fabricated by different compaction temperatures and pressures are used to compare the effect of porosity in 2-D and 3-D coatings and these results are shown in Fig. 4(a) and (b). The lower the compaction temperature and pressure are, the higher the porosity [13] becomes. Fig. 4(a) shows the variation of heat flux for #143 and #150 with $\lambda_m = 1.0$ mm as well as the result for #300 [11] with $\lambda_m = 1.53$ mm. The three surfaces reach at a similar q_{CHF}, but the slope is reduced as porosity increases. As $\langle k \rangle$ increases, the wick superheat is reduced. Fig. 4(b) shows a similar results for #145 and #147, which both have $\lambda_m = 1.9$ mm.

Considering the 2-D and 3-D modulated porous coatings as packed particles with particles being in contact with each other [14,15], an empirical relation for the effective thermal conductivity $\langle k \rangle$ as a function of ϵ in randomly arranged solid–fluid phases is [18]

$$\frac{\langle k \rangle}{k_f} = \frac{k_s}{k_f}^{0.280 - 0.757 \log(\epsilon) - 0.057 \log k_s/k_f} \qquad 0.2 < \epsilon \leqslant 0.6. \qquad (1)$$

where k_s and k_f are the thermal conductivity of solid and fluid, respectively. From the relation, for small porosity, the slope is increased due to the increment of $\langle k \rangle$. However, porosity is not likely related to q_{CHF}. The results for the effect of porosity are listed in Table 2.

3.2. Effect of particle diameter

To study the effect of particle diameter on q_{CHF}, $d_p = 100$ μm from surface #243, #246, and #250, as well as $d_p = 200$ μm from surface #150, are used. Surfaces #150 and #243 are fabricated under the same compaction temperature and pressure, but #243 has lower porosity ($\epsilon = 0.22$) due to its small particle diameter. Fig. 5 shows the measured q with respect to the wick superheat. The q_{CHF} for #150, #243, #246, and #250 varies from 638 kW/m² to 815 kW/m². The q_{CHF} for #246 is the lowest (638 kW/m²) which

Fig. 5. Same as Fig. 4, but showing variation of particle diameter for surfaces #243, #246 and #250 with $d_p = 100\ \mu m$, as well as #150 with $d_p = 200\ \mu m$.

Fig. 6. Variation of measured heat flux with respect to wick superheat for different coatings having the same geometrized parameters, $\langle d_p \rangle = 200\ \mu m$, $\langle \epsilon \rangle = 0.29 - 0.30$, $\langle l \rangle = 2.00$ mm, $\langle w \rangle = 1.19$ mm, $\lambda_m = 1$ mm.

Fig. 4. Variation of surface heat flux (up to q_{CHF}) with respect to wick superheat, for various porosities. (a) Coating #143 and #150 with $\lambda_m = 1.0$ mm, as well as surface #300 with $\lambda_m = 1.53$ mm. (b) Coating #145 and #147 with $\lambda_m = 1.9$ mm.

might be caused by the flat tips of the stack. Surface #250 reaches maximum q_{CHF}, however, it is difficult to analyze due to the lack of geometric repeatability (same unit cell throughout) and that variation may also be regarded as experimental uncertainty. Overall, this result indicates that q_{CHF} is nearly independent of the particle diameter of the porous coatings.

It also implies that q_{CHF} of the 2-D surfaces can reach at as high as q_{CHF} under the 3-D single and dual modulation [11]. According to the Squire theorem [16], the most unstable perturbation is 2-D due to its shear flow. Also for the marginal instability (i.e., the onset of instability which is generally treated using the linear stability theory, as compared to the growth of such nonlinear unstable modes), this theorem shows that for the 2-D and 3-D Rayleigh–Taylor Instability with similar initial conditions, the 2-D cases produce roughly comparable growth rates to 3-D cases in the early stages of nonlinear growth [17]. Therefore, we expect the 2-D modulation produces similar hydrodynamic instability results as the 3-D modulation presented in previous study [11].
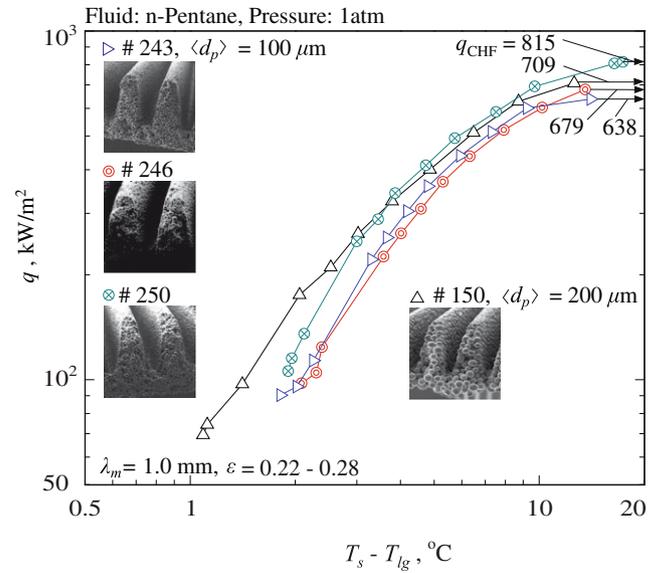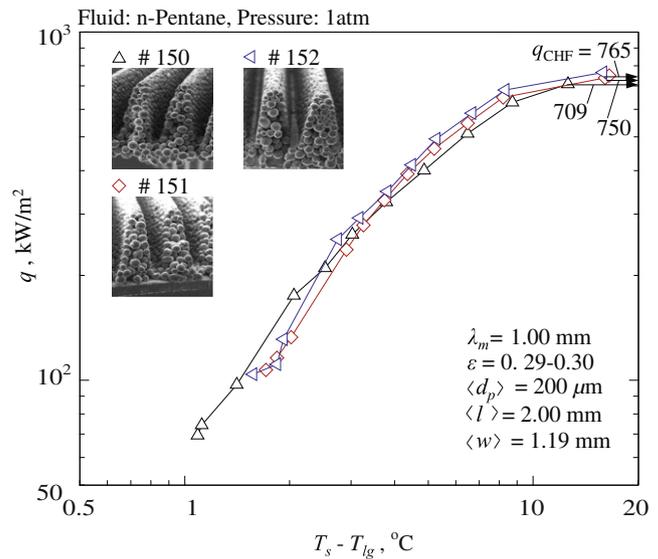
3.3. Reproducibility of coatings

In Fig. 6, surfaces #151 and #152, fabricated under the same conditions as surface #150 are tested and repeatable results were obtained for the 2-D modulated coatings.

3.4. 3-D coatings with small aspect ratio

Using different tooling, 3-D modulated coatings with stack height $l = 0.71$ mm are tested and their results are shown in Fig. 7. Due to the small aspect ratio less than unity, 3-D coatings are seemed to be uniform coating with short pentahedral pyramid bumps. Two identical surfaces such as #253 and #254, #259 and #262, as well as #264 and #265 are fabricated under the same condition. The overall q_{CHF} of 3-D surfaces with corresponding wick superheat is less than the results of 2-D surfaces and 3-D single
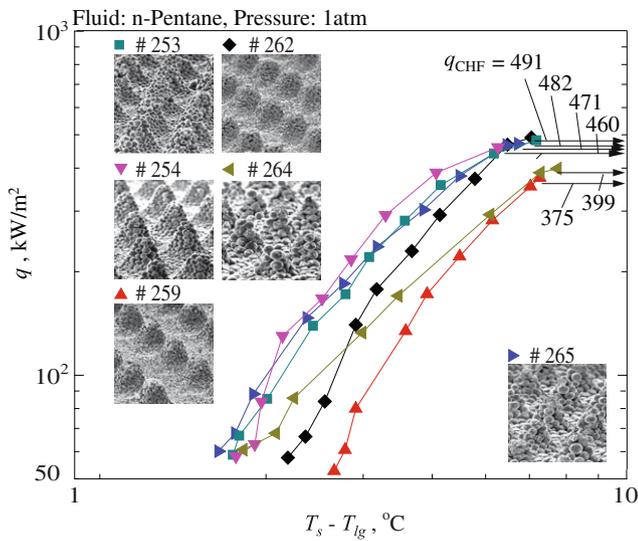
Fig. 7. Variation of measured heat flux with respect to wick superheat for 3-D modulated porous coatings.

and dual modulated coatings [11]. Since the small aspect ratio for 3-D coatings can act as a trap for vapor escaping from the phase change interface, reducing permeability of the liquid which, in turn, causes a small q_{CHF} [4,18]. Although it is unclear how the aspect ratio is related to the q_{CHF} yet, a required aspect ratio might exists to increase the instability of the liquid and vapor flow and increase the q_{CHF}.

3.5. Comparison of 2-D and 3-D coatings

Fig. 8 shows the maximum q_{CHF} of various coatings for comparison. The measured q_{CHF} of the plain surface and for a uniform coating are also included [11]. For 2-D coatings, surface #250 reaches the maximum q_{CHF} (815 kW/m²) and surface #400 [11] for 3-D dual height modulation reaches 762 kW/m². Considering experimental uncertainties mentioned in Section 3.2, the measured q_{CHF} of surface #250 is close to that of #400. Due to the high porosity, the slope of #400 [11] is lower than that of #250 and #262. The
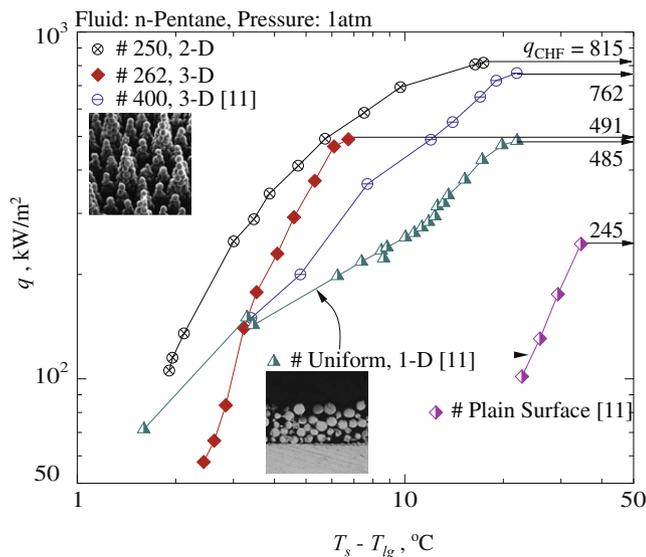
q_{CHF} of #262 is close to the uniform porous layer coating. However, the wick superheat of #262 is the smallest among the surfaces which might give an advantage since reducing the wick superheat is also important. The results for all coatings are summarized in Table 2.

3.6. Effect of modulation wavelength

To investigate the effect of modulation wavelength λ_m, we use surfaces #145, #250, #262, #300, #400 which have different λ_m, a uniform coating and a plain surface. Fig. 9 shows the predicted q_{CHF} from the Zuber hydrodynamic stability theory [10]. The experimental results are also shown. The measured results for surfaces #300 and #400 [11] are in agreement with prediction of the Zuber theory, so are the results of surfaces #145 and #250. The suggested q_{CHF} (i.e., 1.8 times that of plain surface) [12] for the uniform coating with $\epsilon = 0.4$ and $d_p = 200$ µm is 478 kW/m² which is based on the measured value of $q_{CHF} = 480$ kW/m². For surface #262, the predicted q_{CHF} is much higher at this λ_m. This is due to the small aspect ratio for #262 (the measured q_{CHF} is close to the suggested value for uniform coating). As mentioned before, this implies that the stack aspect ratio might not be large enough for the theory to apply. The determination of the required l is yet to be done.

The predicted variation of q_{CHF} as a function of λ_m [11] is developed based on the Zuber hydrodynamic stability theory in [10]. Zuber developed a theoretical model for q_{CHF} based on the idealized hydrodynamics of a liquid–vapor interface system above the surface in pool boiling considering the ability to supply liquid to the surface where the vapor escapes. According to the Zuber hydrodynamic stability theory, the portion of the cross-section flow area for vapor escape on the heated area and the critical Rayleigh–Taylor wavelength are crucial in determining q_{CHF}. Zuber hypothesized that the heated area is divided into $A_b = A_g + A_l$, where A_g is the area where the vapor escapes and A_l is the area for liquid covers. The cylindrical vapor channel area of $A_g = \pi R_g^2$, where the radius $R_g = a\lambda_b$, a is ratio of R_g/λ_b, and λ_b is the length scale, i.e., $A_b = \lambda_b^2$. Zuber related the Kelvin–Helmholtz instability wavelength λ_{K-H} and Rayleigh–Taylor wavelength λ_{R-T} through [10]

$$\lambda_{K-H} = \lambda_{R-T} = 2\pi R_g = 2\pi a\lambda_b. \tag{2}$$

Fig. 8. Maximum q_{CHF} with respect to wick superheat, for effective 1-D, 2-D, and 3-D modulated porous coatings.
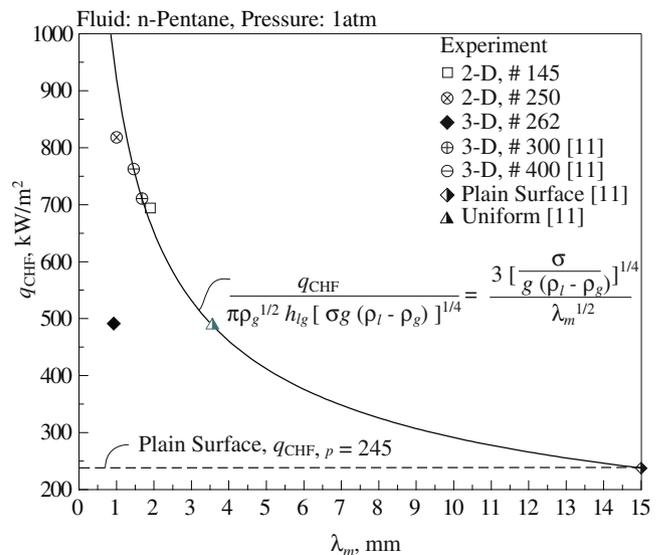

Fig. 9. Variation of the measured q_{CHF} with respect to the modulation wavelength. The results for 3-D single and dual modulation of [11] are also included. The results of prediction of hydrodynamic stability theory are also shown.

Then the relation for q_{CHF} in terms of λ_{K-H} is [11]

$$q_{CHF} = \Delta h_{lg} \left(\frac{2\pi^3 a^4 \sigma \rho_g}{\lambda_{K-H}} \right)^{1/2}, \tag{3}$$

where $a = 1/4$ and $\lambda_{K-H} = 2\pi a \lambda_b = 2\pi a \lambda_m$ [10]. Thus, the final relation is [11]

$$\frac{q_{CHF}}{\pi \rho_g^{1/2} \Delta h_{lg} [\sigma g (\rho_l - \rho_g)]^{1/4}} = \frac{3 \left[\frac{\sigma}{g(\rho_l - \rho_g)} \right]^{1/4}}{\lambda_m^{1/2}}. \tag{4}$$

The above relations clearly indicate that q_{CHF} is inversely proportional to the modulation wavelength $\lambda_m^{1/2}$. As previously mentioned, the 2-D surface modulation results in controlled instability (i.e., λ_m) of the vapor–liquid interfaces, just as 3-D modulation [11] does.

4. Conclusion

We have fabricated 2-D and 3-D modulated (wavelength λ_m) porous coatings using hot-powder compaction and used them for enhanced pool boiling. It is shown that the 2-D coatings behave similar to the 3-D coatings by carbon-molding in modulating the stability of the vapor–liquid interface thus causing increase in the critical heat flux inversely proportional to the square root of λ_m. It is also found that for the surface modulations to be effective, the modulation height should be nearly as large as the wavelength.

Acknowledgements

References

[1] A.E. Bergles, M.C. Chyu, Characteristics of nucleate pool boiling from porous metallic coatings, ASME J. Heat Transfer 104 (1982) 279–285.
[2] J.H. Lienhard, L.C. Witte, An historical review of the hydrodynamic theory of boiling, Rev. Chem. Eng. 3 (3 and 4) (1985) 187–280.
[3] N.H. Afgan, L.A. Jovic, S.A. Kovalev, Boiling heat transfer from surfaces with porous layers, Int. J. Heat Mass Transfer 28 (2) (1985) 279–285.
[4] K.S. Udell, Heat transfer in porous media considering phase change and capillarity – the heat pipe effect, Int. J. Heat Mass Transfer 28 (2) (2006) 485–495.
[5] S.L. Soloviyov, Liquid evaporation heat transfer on a porous surface, Heat Transfer Sov. Res. 18 (3) (1996) 58–64.
[6] S.A. Kovalyo, S.L. Soloviyov, Heat transfer and critical heat fluxes in boiling on a porous surface, Heat Transfer Sov. Res. 22 (3) (1990) 364–375.
[7] A.E. Bergles, M.C. Chyu, Characteristics of nucleate pool boiling from porous metallic coatings, ASME. J. Heat Transfer 104 (1982) (1990) 279–285.
[8] R. Webb, Principles of Enhanced Heat Transfer, Wiley, New York, 1993.
[9] J.Y. Chang, S.M. You, Enhanced boiling heat transfer from micro-porous surfaces: effects of a coating composition and method, Int. J. Heat Mass Transfer 40 (18) (1997) 4449–4460.
[10] N. Zuber, Hydrodynamic Aspects of Boiling Heat Transfer, AECU-4439, Physics and Mathematics, US Atomic Energy Commission, 1959, pp. 1–196.
[11] S.G. Liter, M. Kaviany, Pool-boiling CHF enhancement by modulated porous-layer coating: theory and experiment, Int. J. Heat Mass Transfer 44 (2001) 4287–4311.
[12] G.S. Hwang, M. Kaviany, Critical heat flux in thin, uniform particle coatings, Int. J. Heat Mass Transfer 49 (2006) 844–849.
[13] M. Koç, Y. Usta, A. Karakoç, Investigations on thermo-mechanical fabrication of micro-scale porous surface features, J. Power Sources 179 (2008) 592–602.
[14] M. Kaviany, Principles of Heat Transfer, Wiley, New York, 2001.
[15] A.F. Mills, Basic Heat and Mass Transfer, Prentice Hall, Upper Saddle River, 1999.
[16] A. Deloncle, J. Chomaz, P. Billant, Three-dimensional stability of a horizontally sheared flow in a stably stratified fluid, J. Fluid Mech. 570 (2006) 297–305.
[17] W. Cabot, Comparison of two- and three-dimensional simulations of miscible Rayleigh–Taylor instability, Phys. Fluids 18 (2006) 045101.
[18] M. Kaviany, Principles of Heat Transfer in Porous Media, second ed., Springer, New York, 1995.